Degenerate Motions of Multisensor Fusion-based Navigation

Woosik Lee, Chuchu Chen, and Guoquan Huang

***Abstract*— The system observability analysis is of practical importance, for example, due to its ability to identify the unobservable directions of the estimated state which can influence estimation accuracy and help develop consistent and robust estimators. Recent studies focused on analyzing the observability of the state of various multisensor systems with a particular interest in unobservable directions induced by degenerate motions. However, those studies mostly stay in the specific sensor domain without aiding to extend the understanding to other heterogeneous systems. To this end, in this work, we provide degenerate motion analysis on general local and global sensor-paired systems, offering insights applicable to a wide range of existing navigation systems. Our analysis includes 9 degenerate motion identification including 5 already identified in literature and 4 new motions with both synchronous and asynchronous sensor-pair cases. Comprehensive numerical studies are conducted to verify those identified motions, show the effect of degenerate motion on state estimation, and demonstrate the generalizability of our analysis on various multisensor systems.**

I. Introduction

Consistent and accurate state estimation is a fundamental capability for autonomous robotics, enabling effective planning, control, and perception tasks. This is often addressed by multisensor fusion approaches leveraging complementary information from heterogeneous sensors [1], [2]. Successfully integrating multiple sensing modalities requires the accurate understanding of spatiotemporal relations between them, so-called *spatiotemporal extrinsics*. Consequently, calibrating these extrinsics becomes a critical yet challenging task for achieving high-quality state estimation. Many existing methods assume perfect offline calibration [3]–[5] and which, however, inject unmodelled errors into the estimator, potentially degrading localization performance if the prior calibration was poor or inevitably changed during long-term operation. To this end, many existing works [6]–[9] append the calibration parameters in the state to improve robustness by modeling their uncertainties and jointly estimating them while performing navigation (i.e., online sensor calibration).

Generally, these states are assumed to be observable/recoverable with sensor information. However, recent works show that the observability of the state can vary depending on the robot's motion [10], [11] motivating many researchers to investigate how to identify unobservable directions of the state [12]–[14] or constrain the estimator [15], [16] to avoid gaining information along unobservable directions. Efforts have also been made to analytically identify motion profiles (i.e., degenerate motions) that yield the state to be partially unobservable. Many of the analyses are within visual-inertial navigation system (VINS [17]) territory and [10] is one of the early works that showed the spatial extrinsic parameters between IMU and camera are fully observable under motions with at least two different axes rotation. Other works, such as [18] identified constant acceleration motion and constant velocity motion that make the VINS state partially unobservable with the gravity magnitude and scale, respectively (similar analysis are also shown in [19]). [20] first showed a general condition for the time offset calibration to be observable and identified degenerate motion as constant acceleration without rotation and constant velocity and rotations along the gravity direction (generalized to rolling shutter camera in [21]). One of the most thorough analyses of degenerate motion is [11], which analyzed the VINS state with spatiotemporal calibration parameters and identified 5 motions: 1-axis rotation with 3D translation, pure 3D translation, constant local angular and linear velocities, constant local angular velocity and global linear acceleration, and no motion. This analysis has been extended to the systems that calibrate IMU intrinsic [22], camera intrinsic [23], and multi-IMU & multi-camera [24].

A relatively small number of works have explored degenerate motion analysis with other multisensor systems (e.g., GPS or LiDAR). [25] performed degenerate motion analysis with LiDAR-camera-IMU system identifying the same set of motion profile of [11] that also makes the LiDAR calibration parameters unobservable, [7] analyzed the wheel-camera-IMU system, identifying the subset of the degenerate motions and some additional motion profiles that make the wheel intrinsic state partially unobservable (similar results can be found in [26] with different wheel configurations). Also, there is an analysis of kinematic chained-multi-IMUs finding unique motion that makes their joint center partially unobservable, and [27] presented degenerate motion analysis on the inertial system fused with different geometric feature measurement models (point, line, and plane).

While these findings greatly help in understanding those systems and further aid in designing consistent estimators [28]–[30], the findings stay in the specific analyzed sensor domain, and the extension of those analyses to the other systems remains unclear. To this end, we aim to generalize those analyses to a local and global sensor-paired system where the local sensor (e.g., IMU or wheel encoder) provides 6 DOF ego-motion information while the global pose information can be measured (e.g., GPS) or inferred (i.e., Camera or LiDAR)[1] from the global sensor, that can be generalized to most multisensor systems.

The main contributions of this work include:

- We generalize the existing degenerate motion analysis

This work was partially supported by the University of Delaware (UD) College of Engineering, NSF MRI-2018905, and Google ARCore.

The authors are with the Robot Perception and Navigation Group (RPNG), University of Delaware, Newark, DE 19716, USA. {woosik,ccchu,ghuang}@udel.edu

[1]While these sensors are typically *not* considered as global sensors, they can provide *global information* with map or place recognition.

TABLE I: Summary of degenerate motions. The new findings of the degenerate motion profile are highlighted with bold text.

Degenerate Motions	Partially Unobservable States	References	Lemmas
1 Axis Rotation & 3 Axis Translation	${}^{G}\mathbf{p}_I,\ {}^{J}\mathbf{p}_I$	[7], [11], [25]	*Lemma 1*
Constant Local Linear & Angular Velocities	${}^{G}\mathbf{p}_I,\ {}^{J}_{I}\bar{q},\ {}^{J}\mathbf{p}_I,\ {}^{J}t_I$	[7], [11], [20], [21], [25]	*Lemma 2*
3 Axis Translation	${}^{G}\mathbf{p}_I,\ {}^{J}\mathbf{p}_I$	[7], [11], [25]	*Lemma 3*
2 Axis Translation	${}^{G}\mathbf{p}_I,\ {}^{J}\mathbf{p}_I$	[7], [11], [25]	*Lemma 3*
1 Axis Translation	${}^{I}_{G}\bar{q},\ {}^{G}\mathbf{p}_I,\ {}^{J}_{I}\bar{q},\ {}^{J}\mathbf{p}_I$		***Lemma 4***
Constant Linear Velocity	${}^{I}_{G}\bar{q},\ {}^{G}\mathbf{p}_I,\ {}^{J}_{I}\bar{q},\ {}^{J}\mathbf{p}_I,\ {}^{J}t_I$		***Lemma 5***
1 Axis Rotation	${}^{I}_{G}\bar{q},\ {}^{G}\mathbf{p}_I,\ {}^{J}_{I}\bar{q},\ {}^{J}\mathbf{p}_I$		***Lemma 6***
Constant Angular Velocity	${}^{I}_{G}\bar{q},\ {}^{G}\mathbf{p}_I,\ {}^{J}_{I}\bar{q},\ {}^{J}\mathbf{p}_I,\ {}^{J}t_I$		***Lemma 7***
No Motion	${}^{I}_{G}\bar{q},\ {}^{G}\mathbf{p}_I,\ {}^{J}_{I}\bar{q},\ {}^{J}\mathbf{p}_I,\ {}^{J}t_I$	[7], [11]	*Lemma 8*

to the state of general local and global sensor-paired systems with spatiotemporal calibration that can be applied to broader multisensor systems.

- We perform the analysis for both synchronized and asynchronous systems, identifying 9 degenerate motions including 5 already identified and 4 new (see Tab. I).
- The identified degenerate motions are verified from our numerical study and shown to hurt not only the robot pose estimation but also calibration performance toward exact unobservable directions. The numerical study is extended to various combinations of multisensor systems, including IMU, camera, GPS and LiDAR, showing the generalizability of our analysis to multisensor systems.

II. Synchronous Global and Local Sensor-paired System

In this section, we present preliminaries of a synchronous global-local sensor-paired system for the degenerate motion analysis. Note we use the term *synchronous* to indicate that the two sensor measurements have the same timestamps while the time offset between the sensors still exists that needs to be calibrated. We define two sensors as: $\{I\}$ that provides ego-motion information (e.g., IMU or wheel), and $\{J\}$ that receives global pose measurements (e.g., GPS or motion tracking). We assume noise-free for the analysis.

A. State to Analyze

At time t_k, the state vector carries the current pose of sensor $\{I\}$ and the spatiotemporal calibration parameters:

$$\mathbf{x}_{\mathbf{S}_k} = \begin{bmatrix} {}^{I_k}_{G}\bar{q}^\top & {}^{G}\mathbf{p}_{I_k}^\top & {}^{J}_{I}\bar{q}^\top & {}^{J}\mathbf{p}_I^\top & {}^{J}t_I \end{bmatrix}^\top \tag{1}$$

where ${}^{I_k}_{G}\bar{q}$ is the unit quaternion (${}^{I_k}_{G}\mathbf{R}$ in rotation matrix form) that represents the rotation from the global $\{G\}$ to the sensor $\{I\}$; ${}^{G}\mathbf{p}_{I_k}$ is the sensor $\{I\}$ position in the global $\{G\}$; $\{{}^{J}_{I}\bar{q}, {}^{J}\mathbf{p}_I\}$ and ${}^{J}t_I$ are the extrinsic calibration and time offset between sensor $\{I\}$ and $\{J\}$. Additionally, the corresponding error state vector is:

$$\tilde{\mathbf{x}}_{\mathbf{S}_k} = \begin{bmatrix} {}^{I_k}_{G}\tilde{\boldsymbol{\theta}}^\top & {}^{G}\tilde{\mathbf{p}}_{I_k}^\top & {}^{J}_{I}\tilde{\boldsymbol{\theta}}^\top & {}^{J}\tilde{\mathbf{p}}_I^\top & {}^{J}\tilde{t}_I \end{bmatrix}^\top \tag{2}$$

Note that throughout the paper, $\hat{\mathbf{x}}$ is used to denote the estimate of a random variable $\mathbf{x}$ with $\tilde{\mathbf{x}} = \mathbf{x} \boxminus \hat{\mathbf{x}}$ denotes the error state. For the quaternion error state, we employ JPL multiplicative error [31] and use $\tilde{\boldsymbol{\theta}} \in \mathbb{R}^3$ defined by the error quaternion i.e., $\tilde{\bar{q}} = \bar{q} \otimes \hat{\bar{q}}^{-1} \simeq [\frac{1}{2}\tilde{\boldsymbol{\theta}}^\top \ 1]^\top$. The $\boxplus$ and $\boxminus$ operations map elements to and from a given manifold and equate to simple + and - for vector variables [32].

B. State Propagation Model with Local Sensor $\{I\}$

At time t_{k-1}, we leverage the local sensor's relative pose information, $\{{}^{I_k}_{I_{k-1}}\bar{q}, {}^{I_{k-1}}\mathbf{p}_{I_k}\}$, to propagate the state, Eq. (1), from t_{k-1} to t_k as:

$${}^{I_k}_{G}\bar{q} = {}^{I_k}_{I_{k-1}}\bar{q} \boxplus {}^{I_{k-1}}_{G}\bar{q}, \quad {}^{G}\mathbf{p}_{I_k} = {}^{G}\mathbf{p}_{I_{k-1}} + {}^{G}_{I_{k-1}}\mathbf{R}\,{}^{I_{k-1}}\mathbf{p}_{I_k} \tag{3}$$

while the calibration states remain the same. The corresponding error state transition can be shown as:

$$\tilde{\mathbf{x}}_{\mathbf{S}_k} = \boldsymbol{\Phi}_{\mathbf{S}}(t_k, t_{k-1})\tilde{\mathbf{x}}_{\mathbf{S}_{k-1}} \tag{4}$$

$$\boldsymbol{\Phi}_{\mathbf{S}}(t_k, t_{k-1}) = \begin{bmatrix} {}^{I_k}_{I_{k-1}}\mathbf{R} & \mathbf{0}_3 & \mathbf{0}_{3\times 7} \\ -{}^{G}_{I_{k-1}}\mathbf{R}\lfloor {}^{I_{k-1}}\mathbf{p}_{I_k} \rfloor & \mathbf{I}_3 & \mathbf{0}_{3\times 7} \\ \mathbf{0}_{7\times 3} & \mathbf{0}_{7\times 3} & \mathbf{I}_7 \end{bmatrix} \tag{5}$$

where $\lfloor \cdot \rfloor$ is a skew-symmetric matrix.

C. State Update Model with Global Sensor $\{J\}$

The synchronized global sensor, $\{J\}$, measures the 6 DOF pose of the sensor in global at the state time t_k as:

$$\mathbf{z}_{\mathbf{S}_k} := \begin{bmatrix} {}^{J_k}_{G}\boldsymbol{\theta} \\ {}^{G}\mathbf{p}_{J_k} \end{bmatrix} = \begin{bmatrix} \mathrm{Log}({}^{J}_{I}\mathbf{R}\,{}^{I_k}_{G}\mathbf{R}) \\ {}^{G}\mathbf{p}_{I_k} + {}^{G}_{I_k}\mathbf{R}\,{}^{I}_{J}\mathbf{p}_J \end{bmatrix} := \mathbf{h}(\mathbf{x}_{\mathbf{S}_k}) \tag{6}$$

where ${}^{J_k}_{G}\boldsymbol{\theta} := \mathrm{Log}({}^{J_k}_{G}\mathbf{R})$ and $\mathrm{Log}(\cdot)$ is the SO(3) matrix logarithmic function [33]. Eq. (6) can be linearized at the state estimate $\hat{\mathbf{x}}_{\mathbf{S}_k}$ and the residual is defined as:

$$\tilde{\mathbf{z}}_{\mathbf{S}_k} := \mathbf{z}_{\mathbf{S}_k} - \mathbf{h}(\hat{\mathbf{x}}_{\mathbf{S}_k}) = \mathbf{H}_{\mathbf{S}_k}\tilde{\mathbf{x}}_{\mathbf{S}_k} \tag{7}$$

where $\mathbf{H}_{\mathbf{S}_k}$ is Jacobian matrix of the measurement function:

$$\mathbf{H}_{\mathbf{S}_k} = \begin{bmatrix} {}^{J}_{I}\mathbf{R} & \mathbf{0}_3 & \mathbf{I}_3 & \mathbf{0}_3 & \boldsymbol{\Xi}_{\mathbf{S_1}} \\ -{}^{G}_{I_k}\mathbf{R}\lfloor {}^{I}\mathbf{p}_J \rfloor & \mathbf{I}_3 & -{}^{G}_{I_k}\mathbf{R}\lfloor {}^{I}\mathbf{p}_J \rfloor {}^{I}_{J}\mathbf{R} & -{}^{G}_{I_k}\mathbf{R}\,{}^{I}_{J}\mathbf{R} & \boldsymbol{\Xi}_{\mathbf{S_2}} \end{bmatrix} \tag{8}$$

$$\boldsymbol{\Xi}_{\mathbf{S_1}} = {}^{J}_{I}\mathbf{R}\,{}^{I_k}\boldsymbol{\omega}_{I_k}, \quad \boldsymbol{\Xi}_{\mathbf{S_2}} = {}^{G}\mathbf{v}_{I_k} - {}^{G}_{I_k}\mathbf{R}\lfloor {}^{I}\mathbf{p}_J \rfloor {}^{I_k}\boldsymbol{\omega}_{I_k} \tag{9}$$

where $\mathbf{v}$ and $\boldsymbol{\omega}$ are linear and angular velocities. The detailed derivation can be found in our tech report [34].

D. Observability Matrix

The observability matrix $\mathbf{M}_{\mathbf{S}}$ for the linearized system can be defined as follows [35]:

$$\mathbf{M}_{\mathbf{S}} = \begin{bmatrix} \mathbf{H}_{\mathbf{S}_0}^\top & (\mathbf{H}_{\mathbf{S}_1}\boldsymbol{\Phi}_{\mathbf{S}}(t_1, t_0))^\top & \dots & (\mathbf{H}_{\mathbf{S}_k}\boldsymbol{\Phi}_{\mathbf{S}}(t_k, t_0))^\top \end{bmatrix}^\top \tag{10}$$

For any $k \geq 1$, the k-th block row, $\mathbf{M}_{\mathbf{S}_k}$ can be derived as:

$$\mathbf{M}_{\mathbf{S}_k} := \mathbf{H}_{\mathbf{S}_k}\boldsymbol{\Phi}_{\mathbf{S}}(t_k, t_0) \tag{11}$$

$$= \begin{bmatrix} {}^{J}_{I}\mathbf{R}\,{}^{I_k}_{I_0}\mathbf{R} & \mathbf{0}_3 & \mathbf{I}_3 & \mathbf{0}_3 & \boldsymbol{\Xi}_{\mathbf{S_1}} \\ \boldsymbol{\Xi}_{\mathbf{S_3}} & \mathbf{I}_3 & \boldsymbol{\Xi}_{\mathbf{S_4}} & -{}^{G}_{I_k}\mathbf{R}\,{}^{I}_{J}\mathbf{R} & \boldsymbol{\Xi}_{\mathbf{S_2}} \end{bmatrix} \tag{12}$$

$$\boldsymbol{\Xi}_{\mathbf{S_3}} = -{}^{G}_{I_k}\mathbf{R}\lfloor {}^{I}\mathbf{p}_J \rfloor {}^{I_k}_{I_0}\mathbf{R} - {}^{G}_{I_0}\mathbf{R}\lfloor {}^{I_0}\mathbf{p}_{I_k} \rfloor \tag{13}$$

$$\boldsymbol{\Xi}_{\mathbf{S_4}} = -{}^{G}_{I_k}\mathbf{R}\lfloor {}^{I}\mathbf{p}_J \rfloor {}^{I}_{J}\mathbf{R} \tag{14}$$

If we can find matrix $\mathbf{N}$ that satisfies $\mathbf{M}_{\mathbf{S}_k}\mathbf{N} = \mathbf{0} \ , \forall k \geq 1$, the basis of $\mathbf{N}$ indicate the unobservable directions of the linearized system.

III. Asynchronous Global and Local Sensor-paired System

In this section, we present preliminaries of an asynchronous global-local sensor-paired system for the degenerate motion analysis. Note we use the term *asynchronous* to indicate that the two sensor measurements have different timestamps. In analogy to the synchronous system, we define local sensor $\{I\}$ and global sensor $\{J\}$ for the analysis.

A. State to Analyze

For the asynchronous system, we analyze the following state which is similar to the synchronous sensor state:

$$\mathbf{x}_{\mathbf{A}_k} = \begin{bmatrix} {}^{I_k}_{G}\bar{q}^\top & {}^{G}\mathbf{p}_{I_k}^\top & {}^{I_{k-1}}_{G}\bar{q}^\top & {}^{G}\mathbf{p}_{I_{k-1}}^\top & {}^{J}_{I}\bar{q}^\top & {}^{J}\mathbf{p}_{I}^\top & {}^{J}t_I \end{bmatrix}^\top \quad (15)$$

Note the state has an additional sensor pose $\{{}^{I_{k-1}}_{G}\bar{q}, {}^{G}\mathbf{p}_{I_{k-1}}\}$ at t_{k-1} to handle the asynchronicity. The corresponding error state can now be presented as:

$$\tilde{\mathbf{x}}_{\mathbf{A}_k} = \begin{bmatrix} {}^{I_k}_{G}\tilde{\boldsymbol{\theta}}^\top & {}^{G}\tilde{\mathbf{p}}_{I_k}^\top & {}^{I_{k-1}}_{G}\tilde{\boldsymbol{\theta}}^\top & {}^{G}\tilde{\mathbf{p}}_{I_{k-1}}^\top & {}^{J}_{I}\tilde{\boldsymbol{\theta}}^\top & {}^{J}\tilde{\mathbf{p}}_{I}^\top & {}^{J}\tilde{t}_I \end{bmatrix}^\top \quad (16)$$

B. State Propagation Model with Local Sensor $\{I\}$

The asynchronous system's state propagation matrix $\boldsymbol{\Phi}_{\mathbf{A}}(t_k, t_0)$ is very close to that of the synchronous one which we refer to our report for more details [34].

C. State Update Model with Global Sensor $\{J\}$

Assume we have a pose measurement of sensor $\{J\}$ at time t'_k, where $t_{k-1} \leq t'_k + {}^{J}t_I \leq t_k$. The measurement can be modeled as follows:

$$\mathbf{z}_{\mathbf{A}_k} := \begin{bmatrix} {}^{J_{k'}}_{G}\boldsymbol{\theta} \\ {}^{G}\mathbf{p}_{J_{k'}} \end{bmatrix} = \begin{bmatrix} \mathrm{Log}({}^{J}_{I}\mathbf{R}\,{}^{I_{k'}}_{G}\mathbf{R}) \\ {}^{G}\mathbf{p}_{I_k} + {}^{G}_{I_{k'}}\mathbf{R}\,{}^{I}\mathbf{p}_{J} \end{bmatrix} := \mathbf{h}(\mathbf{x}_{\mathbf{A}_k}) \quad (17)$$

Due to the measurement asynchronicity, the exact pose $\{{}^{I_{k'}}_{G}\mathbf{R}, {}^{G}\mathbf{p}_{I_{k'}}\}$ does not exist in the state vector, but can be approximated with linear interpolation [36]:

$$\begin{aligned} {}^{G}_{I_{k'}}\mathbf{R} =& {}^{G}_{I_{k-1}}\mathbf{R}\mathrm{Exp}(\lambda\ \mathrm{Log}({}^{I_{k-1}}_{G}\mathbf{R}\,{}^{G}_{I_k}\mathbf{R})) && (18)\\ {}^{G}\mathbf{p}_{I_{k'}} =& (1-\lambda)\,{}^{G}\mathbf{p}_{I_{k-1}} + \lambda\,{}^{G}\mathbf{p}_{I_k} && (19)\\ \lambda =& (t'_k + {}^{J}t_I - t_{k-1})/(t_k - t_{k-1}) && (20)\end{aligned}$$

where $\mathrm{Exp}(\cdot)$ is the SO(3) matrix exponential functions [33]. The measurement model can be linearized at the state estimate $\hat{\mathbf{x}}_{\mathbf{A}_k}$ and the residual is defined as:

$$\tilde{\mathbf{z}}_{\mathbf{A}_k} := \mathbf{z}_{\mathbf{A}_k} - \mathbf{h}(\hat{\mathbf{x}}_{\mathbf{A}_k}) = \mathbf{H}_{\mathbf{A}_k}\tilde{\mathbf{x}}_{\mathbf{A}_k} \quad (21)$$

where $\mathbf{H}_{\mathbf{A}_k}$ is the Jacobian matrix of the measurement function with respect to the involved parameters and can be derived as:

$$\mathbf{H}_{\mathbf{A}_k} = \begin{bmatrix} \boldsymbol{\Xi}_{\mathbf{A_1}} & \mathbf{0}_3 & \boldsymbol{\Xi}_{\mathbf{A_1}} & \mathbf{0}_3 & \mathbf{I}_3 & \mathbf{0}_3 & \boldsymbol{\Xi}_{\mathbf{A_1}} \\ \boldsymbol{\Xi}_{\mathbf{A_4}} & \lambda\mathbf{I}_3 & \boldsymbol{\Xi}_{\mathbf{A_5}} & (1-\lambda)\mathbf{I}_3 & \boldsymbol{\Xi}_{\mathbf{A_6}} & \boldsymbol{\Xi}_{\mathbf{A_7}} & \boldsymbol{\Xi}_{\mathbf{A_8}} \end{bmatrix}$$

where the detailed derivation can be found in our report [34].

D. Observability Matrix

Analogous to our earlier derivations (Eq. (12)), the k-th row block of the observability matrix can be defined as:

$$\mathbf{M}_{\mathbf{A}_k} := \mathbf{H}_{\mathbf{A}_k}\boldsymbol{\Phi}_{\mathbf{A}}(t_k, t_0) \quad (22)$$

where the full derivation and the structure are omitted due to limited space, but interested readers can refer to our tech report [34] for more information.

IV. Degenerate Motion Analysis

By analyzing the observability matrix $\mathbf{M}_{\mathbf{S}_k}$ and $\mathbf{M}_{\mathbf{A}_k}$, we identify the following degenerate motions that cause the correlated state parameters to be partially unobservable. Here, we present both synchronous and asynchronous systems' unobservable directions under degenerate motions showing 1) both system shares the same degenerate motions and 2) the state parameters correlated to the unobservable directions are the same. Brief proofs of degenerate motions for the synchronous system are provided while just showing the null space of the asynchronous system for brevity (see [34] for full verification).

Lemma 1: If the system undergoes 1-axis rotation and general 3-axis translation motion, the state is partially unobservable with directions as:

$$\mathbf{N}_1 = \begin{bmatrix} \mathbf{0}_{1\times 3} & \mathbf{k}^\top & \mathbf{0}_{1\times 3} & ({}^{J}_{I}\mathbf{R}\mathbf{k})^\top & 0 \end{bmatrix}^\top \quad (23)$$

where $\mathbf{k}$ is the rotation axis. The state variables correlated to the unobservable directions are: ${}^{G}\mathbf{p}_I,\ {}^{J}\mathbf{p}_I$.

Proof: The motion constraint can be interpreted as the following geometric constraints:

$${}^{I_0}_{G}\mathbf{R}\mathbf{k} = {}^{I_k}_{G}\mathbf{R}\mathbf{k} = \mathbf{k} \quad (24)$$

We can find $\mathbf{N}_1$ is the null space of $\mathbf{M}_{\mathbf{S}_k}$ with the above constraints:

$$\mathbf{M}_{\mathbf{S}_k}\mathbf{N}_1 = \begin{bmatrix} \mathbf{0}_{3\times 1} \\ \mathbf{k} - {}^{G}_{I_k}\mathbf{R}\,{}^{I}_{J}\mathbf{R}\,{}^{J}_{I}\mathbf{R}\mathbf{k} \end{bmatrix} = \mathbf{0}_{6\times 1} \quad (25)$$

This completes the proof. ■

The asynchronous system has the following unobservable directions similar to $\mathbf{N}_1$ under the same condition:

$$\mathbf{N}'_1 = \begin{bmatrix} \mathbf{0}_{1\times 3} & \mathbf{k}^\top & \mathbf{0}_{1\times 3} & \mathbf{k}^\top & \mathbf{0}_{1\times 3} & ({}^{J}_{I}\mathbf{R}\mathbf{k})^\top & 0 \end{bmatrix}^\top \quad (26)$$

Lemma 2: If the system undergoes constant angular and linear velocity motion, the state has an additional unobservable direction $\mathbf{N}_2$ on top of $\mathbf{N}_1$:

$$\mathbf{N}_2 = \begin{bmatrix} \mathbf{0}_{1\times 6} & -({}^{J}_{I}\mathbf{R}\,{}^{I_0}\boldsymbol{\omega}_{I_0})^\top & ({}^{J}_{I}\mathbf{R}\,{}^{I_0}\mathbf{v}_{I_0})^\top & 1 \end{bmatrix} \quad (27)$$

The state variables correlated to the unobservable directions are: ${}^{G}\mathbf{p}_I,\ {}^{J}_{I}\bar{q},\ {}^{J}\mathbf{p}_I,\ {}^{J}t_I$.

Proof: The motion constraint can be interpreted as the following geometric constraints:

$${}^{I_0}_{G}\mathbf{R}\mathbf{k} = {}^{I_k}_{G}\mathbf{R}\mathbf{k} = \mathbf{k},\ {}^{I_k}\mathbf{v}_{I_k} = {}^{I_0}\mathbf{v}_{I_0},\ {}^{I_k}\boldsymbol{\omega}_{I_k} = {}^{I_0}\boldsymbol{\omega}_{I_0} \quad (28)$$

We can find $\mathbf{N}_2$ is the null space of $\mathbf{M}_{\mathbf{S}_k}$ with the above constraints (only showing the new directions):

$$\mathbf{M}_{\mathbf{S}_k}\mathbf{N}_2 = \begin{bmatrix} -{}^{J}_{I}\mathbf{R}\,{}^{I_0}\boldsymbol{\omega}_{I_0} + {}^{J}_{I}\mathbf{R}\,{}^{I_k}\boldsymbol{\omega}_{I_k} \\ -{}^{G}_{I_k}\mathbf{R}\,{}^{I_0}\mathbf{v}_{I_0} + {}^{G}\mathbf{v}_{I_k} \end{bmatrix} = \mathbf{0}_{6\times 1} \quad (29)$$

This completes the proof. ■

The asynchronous system has the following unobservable directions similar to $\mathbf{N}_2$ under the same condition:

$$\mathbf{N}'_2 = \begin{bmatrix} \mathbf{0}_{1\times 12} & -({}^{J}_{I}\mathbf{R}\,{}^{I_0}\boldsymbol{\omega}_{I_0})^\top & ({}^{J}_{I}\mathbf{R}\,{}^{I_0}\mathbf{v}_{I_0})^\top & 1 \end{bmatrix}^\top \quad (30)$$

Lemma 3: If the system undergoes pure 3D translation or 2D translation (planar) motion, the state has partially unobservable directions that incorporate $\mathbf{N}_1$ as:

$$\mathbf{N}_3 = \begin{bmatrix} \mathbf{0}_3 & \mathbf{I}_3 & \mathbf{0}_3 & ({}^{J}_{I}\mathbf{R}\,{}^{I_0}_{G}\mathbf{R})^\top & \mathbf{0}_{3\times 1} \end{bmatrix} \quad (31)$$

The state variables correlated to the unobservable directions are: ${}^{G}\mathbf{p}_I,\ {}^{J}\mathbf{p}_I$.

Proof: The motion constraint can be interpreted as the following geometric constraints:

$$ {}^{I_0}_{G}\mathbf{R} = {}^{I_k}_{G}\mathbf{R}, \quad {}^{I_k}\boldsymbol{\omega}_{I_k} = {}^{I_0}\boldsymbol{\omega}_{I_0} = \mathbf{0}_{3\times 1} \tag{32} $$

We can find $\mathbf{N}_3$ is the null space of $\mathbf{M}_{\mathbf{S}_k}$ with the above constraints:

$$ \mathbf{M}_{\mathbf{S}_k}\mathbf{N}_3 = \begin{bmatrix} \mathbf{0}_3 \\ \mathbf{I}_3 - {}^{G}_{I_k}\mathbf{R}{}^{I}_{J}\mathbf{R}{}^{J}_{I}\mathbf{R}{}^{I_0}_{G}\mathbf{R} \end{bmatrix} = \mathbf{0}_{6\times 1} \tag{33} $$

This completes the proof. ■

The asynchronous system has the following unobservable directions similar to $\mathbf{N}_3$ under the same condition:

$$ \mathbf{N}'_3 = \begin{bmatrix} \mathbf{0}_3 & \mathbf{I}_3 & \mathbf{0}_3 & \mathbf{I}_3 & \mathbf{0}_3 & ({}^{J}_{I}\mathbf{R}{}^{I_0}_{G}\mathbf{R})^\top & \mathbf{0}_{3\times 1} \end{bmatrix} \tag{34} $$

Lemma 4: If the system undergoes general local 1-axis translation (straight line motion with general velocity) without rotation, the state has an additional unobservable direction $\mathbf{N}_4$ on top of $\mathbf{N}_3$ and $\mathbf{N}_1$:

$$ \mathbf{N}_4 = \begin{bmatrix} \mathbf{k}^\top & \mathbf{0}_{1\times 3} & -({}^{J}_{I}\mathbf{R}\mathbf{k})^\top & \mathbf{0}_{1\times 3} & 0 \end{bmatrix}^\top \tag{35} $$

where $\mathbf{k}$ is the axis of the translation. The state variables correlated to the unobservable directions are: ${}^{I}_{G}\bar{q}$, ${}^{G}\mathbf{p}_I$, ${}^{J}_{I}\bar{q}$, ${}^{J}\mathbf{p}_I$.

Proof: The motion constraint can be interpreted as the following geometric constraints:

$$ {}^{I_0}_{G}\mathbf{R} = {}^{I_k}_{G}\mathbf{R}, {}^{I_k}\boldsymbol{\omega}_{I_k} = {}^{I_0}\boldsymbol{\omega}_{I_0} = \mathbf{0}_{3\times 1}, {}^{I_0}\mathbf{p}_{I_k} = f(t_k)\mathbf{k} \tag{36} $$

where $f(\cdot)$ is a scalar function. We can find $\mathbf{N}_4$ is the null space of $\mathbf{M}_{\mathbf{S}_k}$ with the above constraints (only showing the new directions):

$$ \begin{aligned} \mathbf{M}_{\mathbf{S}_k}\mathbf{N}_4 &= \begin{bmatrix} {}^{J}_{I}\mathbf{R}{}^{I_k}_{I_0}\mathbf{R}\mathbf{k} - {}^{J}_{I}\mathbf{R}\mathbf{k} \\ -{}^{G}_{I_k}\mathbf{R}\lfloor {}^{I}\mathbf{p}_J \rfloor \mathbf{k} - {}^{G}_{I_0}\mathbf{R}\lfloor {}^{I_0}\mathbf{p}_{I_k} \rfloor \mathbf{k} + {}^{G}_{I_k}\mathbf{R}\lfloor {}^{I}\mathbf{p}_J \rfloor \mathbf{k} \end{bmatrix} \\ &= \begin{bmatrix} \mathbf{0}_{3\times 1} \\ -{}^{G}_{I_0}\mathbf{R}\lfloor f(t_k)\mathbf{k} \rfloor \mathbf{k} \end{bmatrix} = \mathbf{0}_{6\times 1} \end{aligned} \tag{37} $$

This completes the proof. ■

The asynchronous system has the following unobservable directions similar to $\mathbf{N}_4$ under the same condition:

$$ \mathbf{N}'_4 = \begin{bmatrix} \mathbf{k}^\top & \mathbf{0}_{1\times 3} & \mathbf{k}^\top & \mathbf{0}_{1\times 3} & -({}^{J}_{I}\mathbf{R}\mathbf{k})^\top & \mathbf{0}_{1\times 3} & 0 \end{bmatrix}^\top \tag{38} $$

Lemma 5: If the system undergoes constant local linear velocity motion (straight line motion with constant velocity) without rotation, the state has additional unobservable direction $\mathbf{N}_5$ on top of $\mathbf{N}_4$, $\mathbf{N}_3$, and $\mathbf{N}_1$ as:

$$ \mathbf{N}_5 = \begin{bmatrix} \mathbf{0}_{1\times 3} & -{}^{G}\mathbf{v}^\top_{I_0} & \mathbf{0}_{1\times 6} & 1 \end{bmatrix}^\top \tag{39} $$

where $\mathbf{k}$ is the axis of the translation. The state variables correlated to the unobservable directions are: ${}^{I}_{G}\bar{q}$, ${}^{G}\mathbf{p}_I$, ${}^{J}_{I}\bar{q}$, ${}^{J}\mathbf{p}_I$, ${}^{J}t_I$.

Proof: The motion constraint provides the following additional geometric constraint on top of Eq. (36):

$$ {}^{I_k}\mathbf{v}_{I_k} = {}^{I_0}\mathbf{v}_{I_0} = s\mathbf{k} \tag{40} $$

where s is the speed of the motion. We can find $\mathbf{N}_5$ is the null space of $\mathbf{M}_{\mathbf{S}_k}$ with the above constraints (only showing the new directions):

$$ \mathbf{M}_{\mathbf{S}_k}\mathbf{N}_5 = \begin{bmatrix} \mathbf{0}_{3\times 1} \\ -{}^{G}\mathbf{v}_{I_0} + {}^{G}\mathbf{v}_{I_k} \end{bmatrix} = \mathbf{0}_{6\times 1} \tag{41} $$

This completes the proof. ■

The asynchronous system has the following unobservable directions similar to $\mathbf{N}_5$ under the same condition:

$$ \mathbf{N}'_5 = \begin{bmatrix} \mathbf{0}_{1\times 3} & -{}^{G}\mathbf{v}^\top_{I_0} & \mathbf{0}_{1\times 3} & -{}^{G}\mathbf{v}^\top_{I_0} & \mathbf{0}_{1\times 6} & 1 \end{bmatrix}^\top \tag{42} $$

Lemma 6: If the system undergoes general 1-axis rotation motion without translation, the state has additional unobservable direction $\mathbf{N}_6$ on top of $\mathbf{N}_1$ as:

$$ \mathbf{N}_6 = \begin{bmatrix} \mathbf{0}_{1\times 3} & \mathbf{k}^\top & \mathbf{0}_{1\times 3} & ({}^{J}_{I}\mathbf{R}\mathbf{k})^\top & 0 \end{bmatrix}^\top \tag{43} $$

where $\mathbf{k}$ is the rotation axis. The state variables correlated to the unobservable directions are: ${}^{I}_{G}\bar{q}$, ${}^{G}\mathbf{p}_I$, ${}^{J}_{I}\bar{q}$, ${}^{J}\mathbf{p}_I$.

Proof: The motion constraint can be interpreted as the following geometric constraints:

$$ {}^{I_0}_{G}\mathbf{R}\mathbf{k} = {}^{I_k}_{G}\mathbf{R}\mathbf{k} = \mathbf{k}, {}^{I_0}\mathbf{p}_{I_k} = \mathbf{0}_{3\times 1}, {}^{I_k}\mathbf{v}_{I_k} = {}^{I_0}\mathbf{v}_{I_0} = \mathbf{0}_{3\times 1} \tag{44} $$

We can find $\mathbf{N}_6$ is the null space of $\mathbf{M}_{\mathbf{S}_k}$ with the above constraints (only showing the new directions):

$$ \mathbf{M}_{\mathbf{S}_k}\mathbf{N}_6 = \begin{bmatrix} \mathbf{0}_{3\times 1} \\ \mathbf{k} - {}^{G}_{I_k}\mathbf{R}{}^{I}_{J}\mathbf{R}{}^{J}_{I}\mathbf{R}\mathbf{k} \end{bmatrix} = \mathbf{0}_{6\times 1} \tag{45} $$

This completes the proof. ■

The asynchronous system has the following unobservable directions similar to $\mathbf{N}_6$ under the same condition:

$$ \mathbf{N}'_6 = \begin{bmatrix} \mathbf{0}_{1\times 3} & \mathbf{k}^\top & \mathbf{0}_{1\times 3} & \mathbf{k}^\top & \mathbf{0}_{1\times 3} & ({}^{J}_{I}\mathbf{R}\mathbf{k})^\top & 0 \end{bmatrix}^\top \tag{46} $$

Lemma 7: If the system undergoes constant 1-axis angular velocity motion without translation, the state has additional unobservable direction $\mathbf{N}_7$ on top of $\mathbf{N}_6$ and $\mathbf{N}_1$ as:

$$ \mathbf{N}_7 = \begin{bmatrix} -{}^{I_0}\boldsymbol{\omega}^\top_{I_0} & \mathbf{0}_{1\times 9} & 1 \end{bmatrix}^\top \tag{47} $$

The state variables correlated to the unobservable directions are: ${}^{I}_{G}\bar{q}$, ${}^{G}\mathbf{p}_I$, ${}^{J}_{I}\bar{q}$, ${}^{J}\mathbf{p}_I$, ${}^{J}t_I$.

Proof: The motion constraint provides the following additional geometric constraint on top of Eq. (44):

$$ {}^{I_k}\boldsymbol{\omega}_{I_k} = {}^{I_0}\boldsymbol{\omega}_{I_0} = s\mathbf{k} \tag{48} $$

where s is the speed of the motion. We can find $\mathbf{N}_7$ is the null space of $\mathbf{M}_{\mathbf{S}_k}$ with the above constraints (only showing the new directions):

$$ \mathbf{M}_{\mathbf{S}_k}\mathbf{N}_7 = \begin{bmatrix} {}^{J}_{I}\mathbf{R}(-{}^{I_0}\boldsymbol{\omega}_{I_0} + {}^{I_k}\boldsymbol{\omega}_{I_k}) \\ {}^{G}_{I_k}\mathbf{R}\lfloor {}^{I}\mathbf{p}_J \rfloor ({}^{I_k}_{I_0}\mathbf{R}{}^{I_0}\boldsymbol{\omega}_{I_0} - {}^{I_k}\boldsymbol{\omega}_{I_k}) \end{bmatrix} = \mathbf{0}_{6\times 1} \tag{49} $$

This completes the proof. ■

The asynchronous system has the following unobservable directions similar to $\mathbf{N}_7$ under the same condition:

$$ \mathbf{N}'_7 = \begin{bmatrix} -{}^{I_0}\boldsymbol{\omega}^\top_{I_0} & \mathbf{0}_{1\times 3} & -{}^{I_0}\boldsymbol{\omega}^\top_{I_0} & \mathbf{0}_{1\times 9} & 1 \end{bmatrix}^\top \tag{50} $$

Lemma 8: If the system has no motion, the state has unobservable directions $\mathbf{N}_8$ and $\mathbf{N}_9$ on top of $\mathbf{N}_3$ as:

$$ \mathbf{N}_8 = \begin{bmatrix} \mathbf{I}_3 & \mathbf{0}_3 & -{}^{J}_{I}\mathbf{R}^\top & \mathbf{0}_{3\times 6} \end{bmatrix}^\top, \mathbf{N}_9 = \begin{bmatrix} \mathbf{0}_{1\times 12} & 1 \end{bmatrix}^\top $$

The state variables correlated to the unobservable directions are: ${}^{I}_{G}\bar{q}$, ${}^{G}\mathbf{p}_I$, ${}^{J}_{I}\bar{q}$, ${}^{J}\mathbf{p}_I$, ${}^{J}t_I$.

Proof: The motion constraint can be interpreted as the following geometric constraints:

$$ {}^{I_0}_{G}\mathbf{R} = {}^{I_k}_{G}\mathbf{R}, \quad {}^{I_k}\boldsymbol{\omega}_{I_k} = {}^{I_0}\boldsymbol{\omega}_{I_0} = \mathbf{0}_{3\times 1} \tag{51} $$

$$ {}^{I_0}\mathbf{p}_{I_k} = \mathbf{0}_{3\times 1}, \quad {}^{I_k}\mathbf{v}_{I_k} = {}^{I_0}\mathbf{v}_{I_0} = \mathbf{0}_{3\times 1} \tag{52} $$

We can find $\mathbf{N}_8$ and $\mathbf{N}_9$ are the null space of $\mathbf{M}_{\mathbf{S}_k}$ with the above constraints (only showing the new directions):

$$ \mathbf{M}_{\mathbf{S}_k}\mathbf{N}_8 = \begin{bmatrix} {}^{J}_{I}\mathbf{R}{}^{I_k}_{I_0}\mathbf{R} - {}^{J}_{I}\mathbf{R} \\ -{}^{G}_{I_k}\mathbf{R}\lfloor {}^{I}\mathbf{p}_J \rfloor {}^{I_k}_{I_0}\mathbf{R} + {}^{G}_{I_k}\mathbf{R}\lfloor {}^{I}\mathbf{p}_J \rfloor \end{bmatrix} = \mathbf{0}_{6\times 3} \tag{53} $$

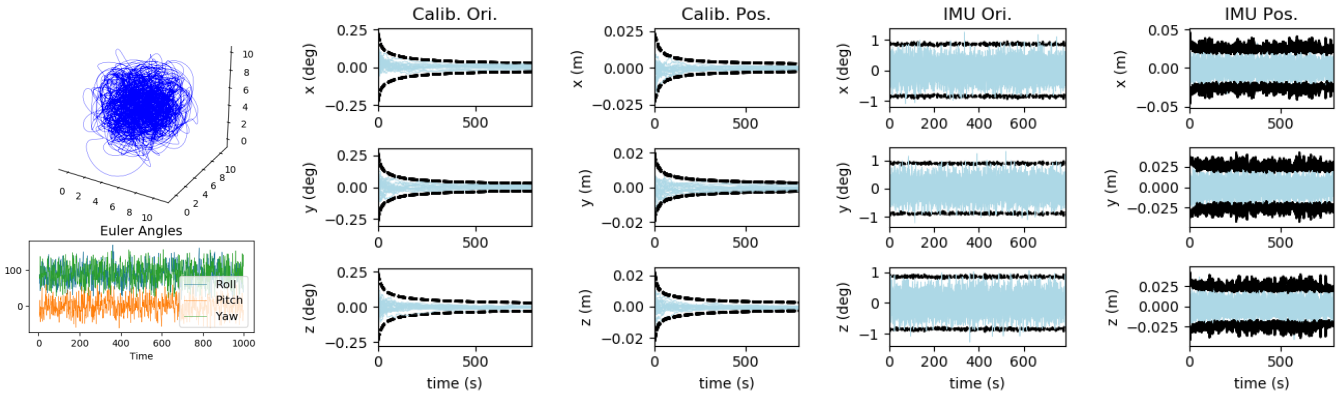

Fig. 1: General Motion Trajectory (left) and State Estimation performance with Online calibration

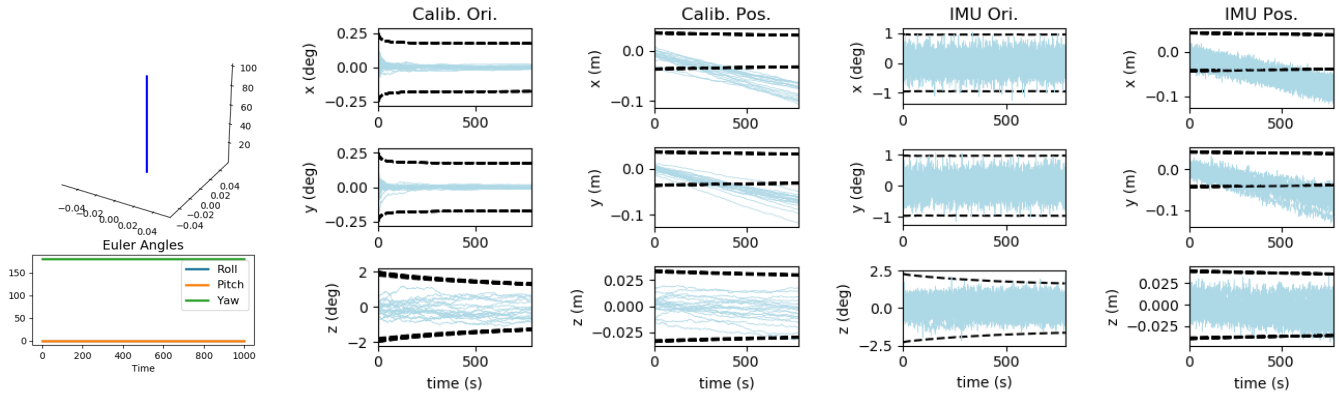

Fig. 2: Constant Linear Velocity Trajectory (left) and State Estimation performance with Online calibration

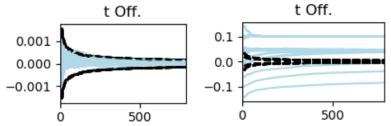

Fig. 3: Time offset calibration with general motion (left) and constant linear velocity motion (right).

$$\mathbf{M}_{\mathbf{S}_k}\mathbf{N}_9 = \begin{bmatrix} {}^{J}_{I}\mathbf{R}^{I_k}\boldsymbol{\omega}_{I_k} \\ {}^{G}\mathbf{v}_{I_k} - {}^{G}_{I_k}\mathbf{R}\lfloor {}^{I}\mathbf{p}_{J}\rfloor {}^{I_k}\boldsymbol{\omega}_{I_k} \end{bmatrix} = \mathbf{0}_{6\times 1} \tag{54}$$

This completes the proof. ■

The asynchronous system has the following unobservable directions similar to $\mathbf{N}_8$ and $\mathbf{N}_9$ under the same condition:

$$\mathbf{N}'_8 = \begin{bmatrix} \mathbf{I}_3 & \mathbf{0}_3 & \mathbf{I}_3 & \mathbf{0}_3 & -{}^{J}_{I}\mathbf{R}^{\top} & \mathbf{0}_{3\times 4} \end{bmatrix}^{\top},\ \mathbf{N}'_9 = \begin{bmatrix} \mathbf{0}_{1\times 18} & 1 \end{bmatrix}^{\top}$$

V. Numerical Study

We conducted a detailed numerical analysis to validate the findings from the prior section. By leveraging OpenVINS [37] simulator and MINS [38], we simulate realistic inertial angular velocity and acceleration measurements as the local motion sensor to perform state propagation. We also simulate an asynchronous global navigation sensor that measures the 6 DoF pose of the sensor [See Eq. (6)]. Note we added noises to the measurements to show how unobservable parameters are estimated under realistic scenarios. For our experiments, we designed multiple degenerate trajectories and offer concrete evidence backing our analytical conclusions and discoveries. Due to the space limit, we only show a few representative results while more results can be found in our tech report [34].

A. Degenerate Motion Validation

Figure 1 and Figure 2 show the trajectories of general and degenerate constant linear velocity motions, and the state estimation with online calibration performance where the blue lines are the estimation error, and black lines indicate the $\pm 3\sigma$ bounds. Figure 3 shows the time offset calibration results of both motions. Table II further report the The average Root Mean Squared Error (RMSE) for the IMU pose and the mean of the calibration parameter errors across 20 Monte-Carlo simulations with different motion profiles.

From the figures, it is evident that during general motion, both the robot state estimation and online calibration are consistent, as their errors remaining within the $\pm 3\sigma$ bounds [See Figure 1 and Figure 3 (left)]. Conversely, in scenarios with constant linear velocity—a motion proven to be degenerate (refer to *Lemma 5*) - the system exhibits inconsistency and inaccuracy in both state estimation and calibration, as depicted in Figure 2 and the right of Figure 3. Both rapidly diverge and become inconsistent as they exceed the $\pm 3\sigma$ bounds. This can also be seen from Table II. When comparing general and constant velocity motion results, the calibration parameters and IMU pose estimates are inaccurate for the constant velocity case.

One interesting observation is the drift direction of both the calibration and state estimation is shown to be the same, for example the sensor and IMU position [See Figure 2, second and last]. This is conjectured to have unobservable directions $\mathbf{N}_3 = \begin{bmatrix} \mathbf{0}_3 & \mathbf{I} & \mathbf{0}_3 & \mathbf{I} & \mathbf{0}_{3\times 1} \end{bmatrix}^{\top}$ due to simulation setup (${}^{J}_{I}\mathbf{R}\,{}^{I_0}_{G}\mathbf{R} = \mathbf{I}_3$), which matches the direction of the drift

TABLE II: Average RMSE values for the IMU pose and calibration parameters (mean error) based on 20 Monte-Carlo runs. Each parameter is represented in three columns for the x, y, and z axes. Entries in bold signify pronounced errors and inconsistencies indicative of the degeneration motion effects.

	${}^{I}_{G}\tilde{\boldsymbol{\theta}}$ RMSE (deg.)			${}^{G}\tilde{\mathbf{p}}_{I}$ RMSE (m)			${}^{J}_{I}\tilde{\boldsymbol{\theta}}$ RMSE (deg.)			${}^{J}\tilde{\mathbf{p}}_{I}$ RMSE (cm)			${}^{J}\tilde{t}_{I}$ (s)
General Motion	0.481	0.481	0.536	0.014	0.014	0.014	0.0048	0.0011	0.0022	0.146	0.160	0.121	6.07e-05
1 Axis Rot. 3 Axis Trans	0.493	0.547	0.471	0.019	0.047	0.016	0.0020	0.0038	0.0020	0.090	0.094	2.374	-
Const Local Linear and Angular Vel.	0.705	0.634	0.682	0.074	0.057	0.055	0.1237	0.1900	1.9096	1.906	4.944	0.561	3.74e-02
1 Axis Trans.	0.603	0.915	0.654	0.095	0.091	0.101	0.0074	0.0031	0.0196	5.776	5.595	3.028	-
Const. Linear Vel.	0.667	0.752	0.924	0.084	0.078	0.063	0.0013	0.0001	0.1681	4.409	3.811	0.804	3.19e-02
1 Axis Rotation	0.598	0.588	0.677	0.033	0.035	0.041	0.0075	0.0046	0.0796	0.081	0.074	2.960	-
Constant Angular Vel.	0.661	0.537	0.810	0.073	0.073	0.060	0.0027	0.0024	0.0844	4.364	3.803	0.801	3.08e-02
No Motion	0.673	0.710	0.868	0.084	0.083	0.063	0.0017	0.0007	0.1488	4.459	3.737	0.785	2.75e-02

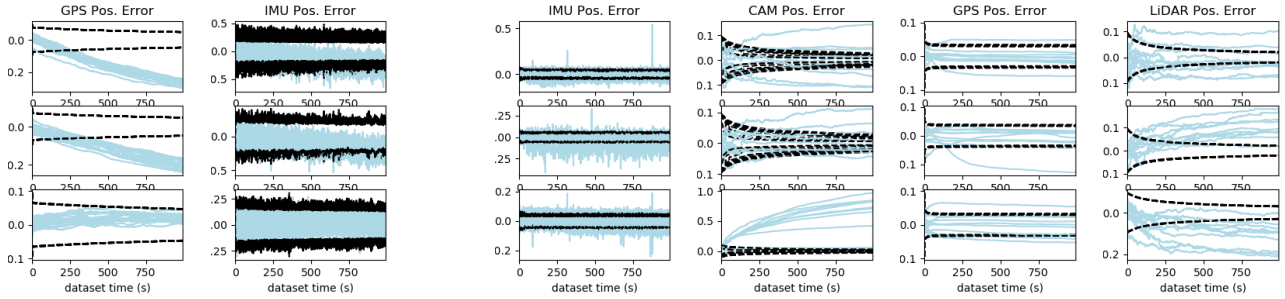

(a) IMU+GPS

(b) IMU+CAMERA+GPS+LiDAR

Fig. 4: State estimation and calibration cross 20 Monte-Carlo simulations during a one-axis translational motion for IMU+GPS (left) and IMU+CAMERA+GPS+LiDAR (right)

(see Table I and *Lemma 3*). These results indicate that the drift in state estimates stemmed from the degenerate motion during calibration.

These results further emphasize the conclusion that since the calibration parameters and state vectors are related and jointly observable, any inconsistency arising from online calibration during degenerate motion directly impacts the performance of state estimation. This is primarily due to the tightly coupled online estimation formulation of state and calibration. This trend is further illustrated in Table II with other degeneration motions as the IMU pose estimation and calibration performance notably drop.

B. The Impact of Noise Level on Estimation Drift

We further perform simulations to explore the impact of degenerate motion under different measurement noise levels. As shown in Figure 5, we use a high-quality IMU and a lower-quality IMU under one axis rotation to perform state estimation with online calibration, The high-quality IMU yielded both accurate and consistent results. There are two reasons behind this. First, a low-noise sensor can provide more information and less randomness. Moreover, enhanced estimation performance means that the linearized estimator has fewer linearization errors. These errors are paramount in causing inconsistencies in the estimator, particularly because of discrepancies in the observability properties (i.e., which causes the wrong information to go into unobservable directions). In essence, it better preserves the system's observability properties.

C. Multi-Sensor System with Online Calibration

We also verified the analysis and evaluate the estimation and calibration performance with different sensors, including IMU, Lidar, Camera, and GPS, where we use the IMU for propagation, and the others can provide an inferred pose measurement as a global sensor. We refer the readers to our previous work [38] about how to model the sensor

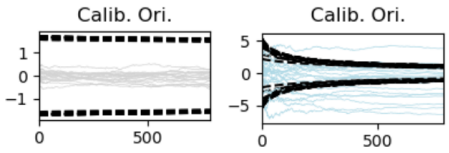

Fig. 5: State estimation and online calibration with constant angular velocity motion paired a good (grey) or a lower-quality IMU (blue)

measurement functions. In our simulation, we pair a Lidar, GPS, or monocular camera with an IMU to enable robot navigation with online calibration. The 20 Monte-Carlo run results are reported in Figure 4. Not surprisingly, all the sensor pairs are shown to suffer from the inconsistency of the degenerate motion.

Moreover, when we employed a system integrating multiple sensors (i.e., a combination of a camera, Lidar, GPS, and IMU, Figure 4b), the results aligned with our expectations. Degenerate motion continued to adversely affect both calibration and navigation performance, even in multi-sensor setups. These findings underscore the applicability of our analysis to be generalized to multi-sensor navigation systems.

VI. Conclusions

In this study, we surveyed the degenerate motion analyses of many systems and further provided comprehensive degenerate motion analysis on local and global sensor-paired systems which can be applied to most multi-sensor setups. Our analysis pinpointed 9 degenerate motions: 5 previously recognized and 4 new ones. Both mathematical proofs and Monte Carlo simulations verified these findings. Through comprehensive numerical studies, we showed the degenerate motion may not only degrade the calibration performance but also hurt the robot pose estimation toward the unobservable direction induced by degenerate motions. We extended our study to multi-sensor systems, showing various combinations of sensor suits are affected by the same degenerate motions verifying the generalizability of our analysis to many multi-sensor systems.

REFERENCES

[1] S. Lynen, M. W. Achtelik, S. Weiss, M. Chli, and R. Siegwart, "A robust and modular multi-sensor fusion approach applied to mav navigation," in *IEEE/RSJ international conference on intelligent robots and systems*, 2013, pp. 3923–3929.

[2] J. K. Hackett and M. Shah, "Multi-sensor fusion: a perspective," in *Proceedings., IEEE International Conference on Robotics and Automation*. IEEE, 1990, pp. 1324–1330.

[3] H. Sun, Y. Jin, M. Fu, J. He, H. Liu, and W.-A. Zhang, "A multisensor-based tightly coupled integrated navigation system," in *2022 5th International Symposium on Autonomous Systems (ISAS)*. IEEE, 2022, pp. 1–6.

[4] T.-M. Nguyen, S. Yuan, M. Cao, T. H. Nguyen, and L. Xie, "Viral slam: Tightly coupled camera-imu-uwb-lidar slam," *arXiv preprint arXiv:2105.03296*, 2021.

[5] X. Meng, H. Wang, and B. Liu, "A robust vehicle localization approach based on gnss/imu/dmi/lidar sensor fusion for autonomous vehicles," *Sensors*, vol. 17, no. 9, p. 2140, 2017.

[6] W. Lee, K. Eckenhoff, P. Geneva, and G. Huang, "Intermittent gps-aided vio: Online initialization and calibration," in *Proc. of the IEEE International Conference on Robotics and Automation*, Paris, France, 2020.

[7] W. Lee, K. Eckenhoff, Y. Yang, P. Geneva, and G. Huang, "Visual-inertial-wheel odometry with online calibration," in *Proc. of the IEEE/RSJ International Conference on Intelligent Robots and Systems*, Las Vegas, NV, 2020.

[8] P. Geneva, N. Merrill, Y. Yang, C. Chen, W. Lee, and G. Huang, "Versatile 3d multi-sensor fusion for lightweight 2d localization," in *Proc. of the IEEE/RSJ International Conference on Intelligent Robots and Systems*, Las Vegas, NV, 2020.

[9] C. Chen, Y. Yang, P. Geneva, W. Lee, and G. Huang, "Visual-inertial-aided online mav system identification," in *Proc. of the IEEE/RSJ International Conference on Intelligent Robots and Systems*, Kyoto, Japan., 2022.

[10] F. M. Mirzaei and S. I. Roumeliotis, "A kalman filter-based algorithm for imu-camera calibration: Observability analysis and performance evaluation," *IEEE transactions on robotics*, vol. 24, no. 5, pp. 1143–1156, 2008.

[11] Y. Yang, P. Geneva, K. Eckenhoff, and G. Huang, "Degenerate motion analysis for aided INS with online spatial and temporal calibration," *IEEE Robotics and Automation Letters (RA-L)*, vol. 4, no. 2, pp. 2070–2077, 2019.

[12] T. Schneider, M. Li, C. Cadena, J. Nieto, and R. Siegwart, "Observability-aware self-calibration of visual and inertial sensors for ego-motion estimation," *IEEE Sensors Journal*, vol. 19, no. 10, pp. 3846–3860, 2019.

[13] K. Hausman, J. Preiss, G. S. Sukhatme, and S. Weiss, "Observability-aware trajectory optimization for self-calibration with application to uavs," *IEEE Robotics and Automation Letters*, vol. 2, no. 3, pp. 1770–1777, 2017.

[14] J. Hernandez, K. Tsotsos, and S. Soatto, "Observability, identifiability and sensitivity of vision-aided inertial navigation," in *2015 IEEE International Conference on Robotics and Automation (ICRA)*. IEEE, 2015, pp. 2319–2325.

[15] J. Lv, X. Zuo, K. Hu, J. Xu, G. Huang, and Y. Liu, "Observability-aware intrinsic and extrinsic calibration of lidar-imu systems," *IEEE Transactions on Robotics*, vol. 38, no. 6, pp. 3734–3753, 2022.

[16] C. Liu, C. Jiang, and H. Wang, "Ingvio: A consistent invariant filter for fast and high-accuracy gnss-visual-inertial odometry," *IEEE Robotics and Automation Letters*, vol. 8, no. 3, pp. 1850–1857, 2023.

[17] G. Huang, "Visual-inertial navigation: A concise review," in *Proc. International Conference on Robotics and Automation*, Montreal, Canada, May 2019.

[18] A. Martinelli, "Vision and imu data fusion: Closed-form solutions for attitude, speed, absolute scale, and bias determination," *IEEE Transactions on Robotics*, vol. 28, no. 1, pp. 44–60, 2011.

[19] K. J. Wu, C. X. Guo, G. Georgiou, and S. I. Roumeliotis, "Vins on wheels," in *2017 IEEE International Conference on Robotics and Automation (ICRA)*. IEEE, 2017, pp. 5155–5162.

[20] M. Li and A. I. Mourikis, "Online temporal calibration for camera–imu systems: Theory and algorithms," *The International Journal of Robotics Research*, vol. 33, no. 7, pp. 947–964, 2014.

[21] J. Huai, Y. Lin, Y. Zhuang, C. K. Toth, and D. Chen, "Observability analysis and keyframe-based filtering for visual inertial odometry with full self-calibration," *IEEE Transactions on Robotics*, vol. 38, no. 5, pp. 3219–3237, 2022.

[22] Y. Yang, P. Geneva, X. Zuo, and G. Huang, "Online imu intrinsic calibration: Is it necessary?" in *Proc. of the Robotics: Science and Systems*, Paris, France, 2020.

[23] ——, "Online self-calibration for visual-inertial navigation: Models, analysis, and degeneracy," *IEEE Transactions on Robotics*, 2023.

[24] Y. Yang, P. Geneva, and G. Huang, "Multi-visual-inertial system: Analysis, calibration and estimation," *arXiv preprint arXiv:2308.05303*, 2023.

[25] X. Zuo, Y. Yang, P. Geneva, J. Lv, Y. Liu, G. Huang, and M. Pollefeys, "Lic-fusion 2.0: Lidar-inertial-camera odometry with sliding-window plane-feature tracking," *arXiv preprint arXiv:2008.07196*, 2020.

[26] X. Zuo, M. Zhang, M. Wang, Y. Chen, G. Huang, Y. Liu, and M. Li, "Visual-based kinematics and pose estimation for skid-steering robots," *IEEE Transactions on Automation Science and Engineering*, 2022.

[27] Y. Yang and G. Huang, "Observability analysis of aided ins with heterogeneous features of points, lines and planes," *IEEE Transactions on Robotics*, vol. 35, no. 6, pp. 399–1418, Dec. 2019.

[28] G. Huang, A. I. Mourikis, and S. I. Roumeliotis, "Observability-based rules for designing consistent EKF SLAM estimators," *International Journal of Robotics Research*, vol. 29, no. 5, pp. 502–528, Apr. 2010.

[29] C. Chen, P. Geneva, Y. Peng, W. Lee, and G. Huang, "Optimization-based vins: Consistency, marginalization, and fej," in *IEEE/RSJ International Conference on Intelligent Robots and Systems (IROS)*, 2023.

[30] C. Chen, Y. Yang, P. Geneva, and G. Huang, "FEJ2: A consistent visual-inertial state estimator design," in *International Conference on Robotics and Automation (ICRA)*, Philadelphia, USA, 2022.

[31] N. Trawny and S. I. Roumeliotis, "Indirect Kalman filter for 3D attitude estimation," University of Minnesota, Dept. of Comp. Sci. & Eng., Tech. Rep., Mar. 2005.

[32] C. Hertzberg, R. Wagner, U. Frese, and L. SchröDer, "Integrating generic sensor fusion algorithms with sound state representations through encapsulation of manifolds," *Information Fusion*, vol. 14, no. 1, pp. 57–77, Jan. 2013.

[33] G. Chirikjian, *Stochastic Models, Information Theory, and Lie Groups, Volume 2: Analytic Methods and Modern Applications*. Springer Science & Business Media, 2011, vol. 2.

[34] W. Lee, C. Chen, and G. Huang, "Technical report: Degenerate motions of multisensor fusion-based navigation," Robot Perception and Navigation Group (RPNG), University of Delaware, Tech. Rep., 2023. [Online]. Available: https://udel.edu/~ghuang/papers/tr_degen.pdf

[35] Z. Chen, K. Jiang, and J. C. Hung, "Local observability matrix and its application to observability analyses," in *[Proceedings] IECON'90: 16th Annual Conference of IEEE Industrial Electronics Society*. IEEE, 1990, pp. 100–103.

[36] M. Li, "Visual-inertial odometry on resource-constrained systems," Ph.D. dissertation, UC Riverside, 2014.

[37] P. Geneva, K. Eckenhoff, W. Lee, Y. Yang, and G. Huang, "Openvins: A research platform for visual-inertial estimation," in *Proc. of the IEEE International Conference on Robotics and Automation*, Paris, France, 2020. [Online]. Available: https://github.com/rpng/open_vins

[38] W. Lee, P. Geneva, C. Chen, and G. Huang, "Mins: Efficient and robust multisensor-aided inertial navigation system," *arXiv preprint arXiv:2309.15390*, 2023. [Online]. Available: https://github.com/rpng/MINS